Journal of Alloys and Compounds 1037 (2025) 182350

Contents lists available at ScienceDirect

Journal of Alloys and Compounds

journal homepage: www.elsevier.com/locate/jalcom

Spin-orbit coupling induced enhancement of upper critical field in superconducting A15 single crystals

Seohee Kim [a], Gichan Son [b], Minsik Kong [a], Youngji Cho [a], Min Jae Kim [a], Huiwon Kim [a], Eun Sang Choi [c], Sangmoon Yoon [d], Jeongwoo Kim [b,*], Jong Mok Ok [a,*]

[a] Department of Physics, Pusan National University, Busan 46241, Republic of Korea
[b] Department of Physics, Incheon National University, Incheon 22150, Republic of Korea
[c] National High Magnetic Field Laboratory, FL 32310, USA
[d] Department of Physics, Gachon University, Gyeonggi-do 13306, Republic of Korea

ARTICLE INFO

Keywords:
A15 superconductor
Ti_3Sb
Nb_3Pt
Single crystal growth
Arc-Czochralski method
Spin-orbit coupling
Upper critical field

ABSTRACT

Spin-orbit coupling (SOC) plays an important role in determining the properties of superconductors and is crucial for designing novel superconducting materials with improved characteristics, including high-performance superconducting wires and topological superconductors for quantum computing. In this study, we systematically investigate the role of SOC in modifying superconducting properties. To this end, A15-structured single crystals of Ti_3Sb and Nb_3Pt, which share identical crystal structures but exhibit significantly different SOC effects, were synthesized using the tetra-arc Czochralski method. A comparative analysis of these materials demonstrates that SOC has a substantial impact on the upper critical field (H_{c2}): the Nb_3Pt single crystal, which has stronger SOC than Ti_3Sb, shows a much higher $H_{c2}(0) \approx H_{c2}^{orb}(0)$ compared to that of Ti_3Sb single crystal, which is $H_{c2}(0) \approx 0.82H_{c2}^{orb}(0)$. These results underscore the significance of SOC as a critical factor in the design and optimization of superconducting materials, highlighting its potential for advancing next-generation applications in high-performance superconducting technologies.

1. Introduction

Spin–orbit coupling (SOC), a fundamental interaction linking an electron's spin with its orbital motion, governs various exotic quantum phenomena, including topological insulators, the spin Hall effect, and the Rashba effect [1–3]. It also plays a crucial role in superconductivity; for example, SOC enables not only topological superconductivity [4] by locking electron spins in a specific direction, thus facilitating the formation of topological Majorana edge states [5], but also high-performance superconductivity by enhancing the upper critical field (H_{c2}) [6]. However, direct experimental studies on its role in superconducting systems remain remarkably limited.

Since the introduction of the Werthamer–Helfand–Hohenberg (WHH) model in 1966 [6], the effect of SOC on the H_{c2} has been a subject of theoretical interest. The H_{c2} is a crucial parameter that governs the stability of the superconducting state and plays a key role in technological applications and material design. Therefore, a deeper understanding of the intricate interplay between SOC and H_{c2} is essential for the development of novel superconductors. Nevertheless, because the strength of SOC is predominantly determined by the atomic number (Z), achieving precise experimental control over SOC remains highly challenging, making it difficult to unambiguously establish its influence on H_{c2}.

The A15 compound family, with over 60 distinct members [7], provides an important model system for studying the correlation between SOC and H_{c2}. A15 compounds crystallize in the cubic space group Pm-3n (No. 223) and typically have the chemical composition A_3B, where A is a transition metal [7]. A15 compounds span a wide range of elements from 3*d* to 5*d* transition metals, providing diverse material choices that enable the design of studies to control SOC while maintaining both structural and superconducting properties.

Many A15 compounds exhibit intriguing superconductivity, with notable examples such as Nb_3Sn [8] and Nb_3Ge [9] achieving high superconducting critical temperatures T_c and H_{c2}. These properties make them promising candidates for advanced technological applications, including tokamak fusion devices, magnetic resonance imaging

* Corresponding authors.
E-mail addresses: kjwlou@inu.ac.kr (J. Kim), okjongmok@pusan.ac.kr (J.M. Ok).

https://doi.org/10.1016/j.jallcom.2025.182350
Received 14 April 2025; Received in revised form 17 June 2025; Accepted 17 July 2025
Available online 18 July 2025
0925-8388/© 2025 Elsevier B.V. All rights are reserved, including those for text and data mining, AI training, and similar technologies.

(MRI) systems, and nuclear magnetic resonance (NMR) equipment [10]. More interestingly, A15 superconductors with 4*d* and 5*d* transition metals exhibit a strong SOC effect, and may host topologically nontrivial band structures [11,12]. This underscores the growing significance of studying A15 compounds, as they offer potential pathways for discovering new topological superconductivity with a large SOC effect.

In this study, we successfully synthesized single crystals of Ti_3Sb and Nb_3Pt with the A15 structure using the tetra-arc Czochralski method, and their crystallinity was confirmed through X-ray diffraction (XRD) analysis. The temperature dependence of $H_{c2}(T)$ was investigated via electrical resistivity measurements under high magnetic fields up to 31 T. Compared to Ti_3Sb, whose H_{c2} is close to the orbital limit (Maki parameter $\alpha \approx 0.7$), Nb_3Pt in the Pauli limit ($\alpha \approx 1.2$) was expected to have a lower H_{c2} due to spin-paramagnetic pair breaking. However, the measured $H_{c2}(0)$ of Nb_3Pt was found to be much closer to its orbital limit field. This discrepancy suggests that SOC significantly influences superconducting properties, highlighting its importance in the development of novel materials such as topological superconductors.

2. Experiment details

Single crystals of Ti_3Sb and Nb_3Pt were grown using the tetra-arc Czochralski method in a custom-built apparatus. To the best of our knowledge, there have been no previous reports on the growth of these materials as single crystals, making this the first successful attempt. The growth of Ti_3Sb and Nb_3Pt single crystals is particularly challenging due to their high melting points and strong reactivity with crucible materials such as Pt, Ir, or oxides. To overcome these difficulties, we utilized a cold crucible and employed the tetra-arc Czochralski method, which is well-suited for growing high-melting-point material [13]. The experimental setup used for the growth process is schematically illustrated in Fig. 1(a).

Polycrystalline samples for single crystal growth were prepared by arc-melting stoichiometric mixtures of Ti (99.9 %, Sigma) or Nb (99.99 %, Sigma) with Sb (99.99 %, Sigma) or Pt (99.9 %, KRTLAB) in an argon atmosphere at a molar ratio of 3:1. To prevent oxidation, the argon purge process was repeated three times by filling the chamber to atmospheric pressure before evacuation. To ensure uniform mixing, the polycrystalline samples were flipped, and the melting process was repeated twice more.

The single crystal growth procedure consists of three main stages: necking, growing, and tailing, as shown in Fig. 1(b) and obtained ingots are presented in Fig. 1(c) and Fig. S1 in Supplementary material. A tungsten rod was used as the seed for the pulling process, with the pulling rate maintained at 1 mm/h after the necking step. To maintain the thermal uniformity of the growing ingot, the crucible and the pulling rod were rotated in opposite directions at speeds of up to 5 rpm. The resulting ingots had diameters of a few millimeters and lengths of a few centimeters. The ingot was confirmed to grow along the [100] direction of the A15 structure. The specimens for the experiments were prepared by cutting the ingots perpendicular to the growth direction using a diamond saw.

The phase purity and crystal structure of the single crystals were analyzed using a powder sample and a powder XRD (X'Pert 3, PANalytical) with Cu-Kα radiation, which is installed at the Quantum Matter Core Facility of Pusan National University. Additionally, XRD (D8 Discover, Bruker) was performed, including $\theta-2\theta$ and scans, to determine the growth direction and crystallinity of the samples. Diffraction data for Ti_3Sb and Nb_3Pt were collected at room temperature using a single crystal X-ray diffractometer (D8 Venture, Bruker) with Mo-Kα radiation. The microstructure of the single crystals was examined using TEM (Tecnai F30, FEI). The magneto transport properties of the crystals were measured using a conventional four-probe configuration with a 12 T TeslatronPT at the Quantum Matter Core Facility of Pusan National University and a 31 T Bitter at the National High Magnetic Field Laboratory in Tallahassee, Florida, USA.

Our DFT computations were conducted using the projected augmented plane-wave method [14,15], as implemented in the Vienna Ab Initio Simulation Package [16]. The Perdew-Burke-Ernzerhof form of the generalized gradient approximation was employed to describe the exchange-correlation interactions among electrons [17]. The energy convergence threshold for the self-consistent field iterations was set to 10^{-5} eV, and the plane-wave basis expansion was truncated at an energy cutoff of 500 eV. A $10 \times 10 \times 10$ **k**-point grid was used to sample the Brillouin zone. The lattice parameters and atomic positions were relaxed until the total energy converged to within 10^{-4} eV. We also included SOC in our calculations to investigate its impact on the low energy states near the Fermi level.

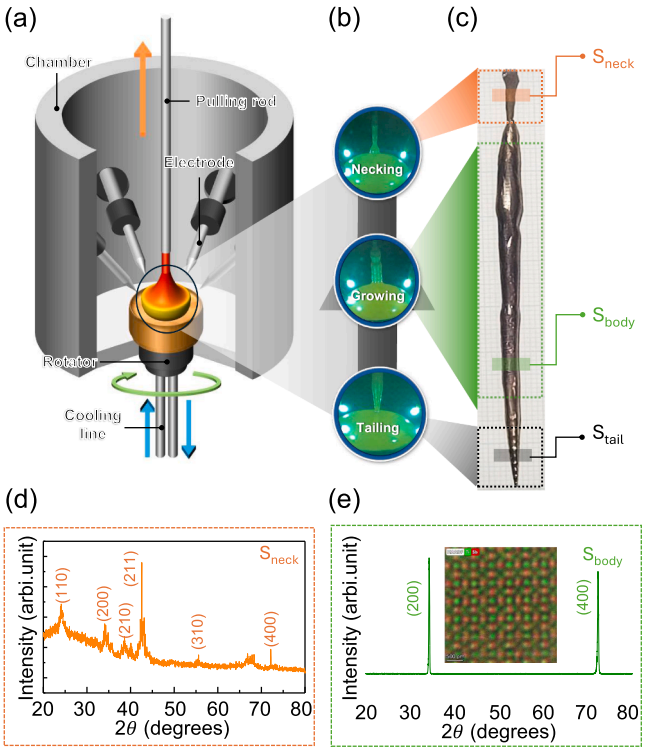

Fig. 1. Crystal growth apparatus and characterization of the grown crystal. (a) Schematic of tetra-arc Czochralski furnace. The starting materials are loaded into a water-cooled copper crucible and melted by arc discharge produced at the electrodes. (b) Schematics of tetra-arc Czochralski growth process, including the stage of necking, growing, and tailing. (c) The optical image of obtained Ti_3Sb single crystal. The crystal consists of three regions: neck, body, and tail, marked by orange, green, and black dashed boxes, respectively. For structure analysis, two marked regions, S_{neck} from the neck and S_{body} from the stably grown body part, were selected. (d) XRD patterns of the S_{neck} show polycrystalline characteristics. (e) XRD patterns of the S_{body} show single crystallinity. The inset in (e) presents a HAADF STEM image of S_{body}.

3. Results and discussion

Under an external magnetic field, superconducting pair breaking is governed by both orbital and spin-paramagnetic effects [18]. The former is related to orbital limiting field, $H_{c2}^{orb}(0)$, which represents the critical field at which vortex cores begin to overlap and is given by: $H_{c2}^{orb}(0) = \Phi_0/2\pi\xi^2$, where ξ is the coherence length and $\Phi_0 = 2.07 \times 10^{-15}$ T•m^2 is the flux quantum. For single-band BCS superconductors, $H_{c2}^{orb}(0)$ is commonly estimated from the slope of the $H-T$ phase boundary at T_c, expressed as: $H_{c2}^{orb}(0) = -0.69|dH_{c2}/dT|_{T_c}T_c$ in the dirty limit [6]. The spin-paramagnetic pair-breaking effect arises from the Zeeman splitting of spin-singlet Cooper pairs. The Pauli-limiting field, H_P, is determined by the balance between the Zeeman energy in the normal state and the superconducting condensation energy, given by: $1/2\chi_N H_P^2 =$

$1/2N(E_F)\Delta^2$, where $\chi_N = g\mu_B^2 N(E_F)$ is the normal-state spin susceptibility, g is the Lande g-factor, μ_B is the Bohr magneton, Δ is the superconducting gap and $N(E_F)$ is the density of state at the Fermi level E_F. For a BCS superconductor, where $2\Delta(0) = 3.52k_BT_c$, the Pauli-limiting field simplifies to: $H_P(0) = 1.84T_c$ [19].

In real materials, H_{c2} is influenced by both orbital and spin-paramagnetic effects. Their relative importance is characterized by the Maki parameter: $\alpha = \sqrt{2}H_{c2}^{orb}(0)/H_P(0)$, which quantifies the competition between orbital and Pauli-limiting effects in determining H_{c2} [20]. When $\alpha < 1$, the orbital limiting effect dominates, allowing $H_{c2}(0)$ to increase up to $H_{c2}^{orb}(0)$, which is primarily determined by the electronic structure. On the other hand, when $\alpha > 1$, the Pauli effect prevails, causing the superconducting state to be destroyed at much lower magnetic fields of $H_P(0)$ before the orbital limiting effect can manifest. In some superconductors, where the Pauli effect significantly reduces H_{c2}, spin-orbit scattering can play a crucial role. According to the WHH model, spin-orbit scattering can help restore the reduced H_{c2} caused by the Pauli effect back toward the orbital limit. This highlights the necessity of considering SOC effects when analyzing superconducting properties.

In order to study the effect of spin-orbit scattering on $H_{c2}(T)$, we chose two A15 superconductors, Ti_3Sb and Nb_3Pt, which have the same structure but are expected to exhibit different SOC effects [21,22]. First, to estimate the strength of SOC in both superconductors and evaluate its influence on the electronic structure, we calculated the band structures of both materials using density functional theory (DFT). Fig. 2(a) and (b) exhibit the band structure near the Fermi level in Ti_3Sb and Nb_3Pt, both with and without SOC. While the low-energy states of Ti_3Sb are marginally affected by the presence of SOC, those of Nb_3Pt undergo significant modifications due to state mixing induced by SOC. We further found that calculations of the electronic susceptibility using the Lindhard formula suggest a possible influence of SOC on superconductivity; detailed results are provided in Fig. S2. This pronounced difference in SOC between Ti_3Sb and Nb_3Pt is particularly significant in identifying the role of SOC in determining H_{c2}, which will be discussed in detail below. The orbital-resolved band structure in Fig. 2(c) demonstrates that the states near the Fermi level primarily originate from Ti atoms in Ti_3Sb, indicating that the insensitivity to SOC arises from the weak atomic SOC of Ti. In Nb_3Pt, the low energy states originate from both Nb and Pt atoms and are strongly hybridized due to the relatively strong SOC of the 5*d* Pt atoms. Therefore, we conclude that specific atomic combination is very crucial for controlling the spin-orbit scattering in A15 materials.

The phase purity and crystal structure of both single crystals were analyzed using XRD and powder XRD. As presented in Fig. 1(c), XRD measurements conducted on different sections of the grown ingot reveal an improvement in crystallinity as the sample undergoes the necking and body-growing stages. We note that these two processes are crucial in single crystal growth, and without them, only polycrystalline samples are obtained, as shown in Fig. S3 in Supplementary material. The crystal formed at the initial growth stage (upper part of ingot) exhibited polycrystallinity due to extensive nucleation induced by thermal shock as shown in Fig. 1(d). In contrast, the lower part of the ingot underwent a solidification process through necking, resulting in the formation of a single crystal structure, as displayed in Fig. 1(e). This suggests that early-stage growth may induce polycrystalline regions, but the optimized process ultimately yields high-quality single crystals. The inset of Fig. 1 (e) shows a high-angle annular dark-field scanning transmission electron microscopy (HAADF STEM) image of the Ti_3Sb single crystal viewed along the [100] zone axis. The HAADF STEM image confirms that high-quality single crystals without twin domains or significant crystal defects were successfully grown. More detailed HAADF STEM images can be found in Fig. S4 in Supplementary material.

Fig. 3(a) and (d) present XRD measurements of Ti_3Sb and Nb_3Pt single crystals, showing Bragg reflections at the (200) and (400) planes. The crystal quality was further assessed via rocking curve analysis at the (200) reflection, yielding FWHM values of $\Delta\omega \approx 0.6^\circ$ for Ti_3Sb and $\Delta\omega \approx 0.3^\circ$ for Nb_3Pt, as shown in Fig. 3(c) and (f). Powder XRD data obtained using crushed single crystals, shown in Fig. 3(b) and (e), confirm an A15 structure with *Pm*-3*n* (No. 223) symmetry. Ti-deficient Ti_2Sb was identified as an impurity in the Ti_3Sb single crystal, as marked in Fig. 3(b), a known impurity previously reported in polycrystalline studies [21]. This indicates minor Ti loss due to volatilization or oxidation. Further structural verification was performed using single-crystal X-ray diffraction (SCXRD), which consistently confirmed cubic structure (*Pm*-3*n*) with lattice parameter $a = 5.2127(1)$ Å for Ti_3Sb and $a = 5.1652(1)$ Å for Nb_3Pt single crystal. The Laue diffraction patterns of Ti_3Sb and Nb_3Pt single crystals are shown in Fig. S5 in Supplementary material, and the refined lattice parameters are summarized in Table 1. Energy-dispersive spectroscopy (EDS) measurements indicated near-stoichiometric elemental ratios (Ti:Sb and Nb:Pt ≈ 3:1) as detailed in Fig. S6 in Supplementary material.

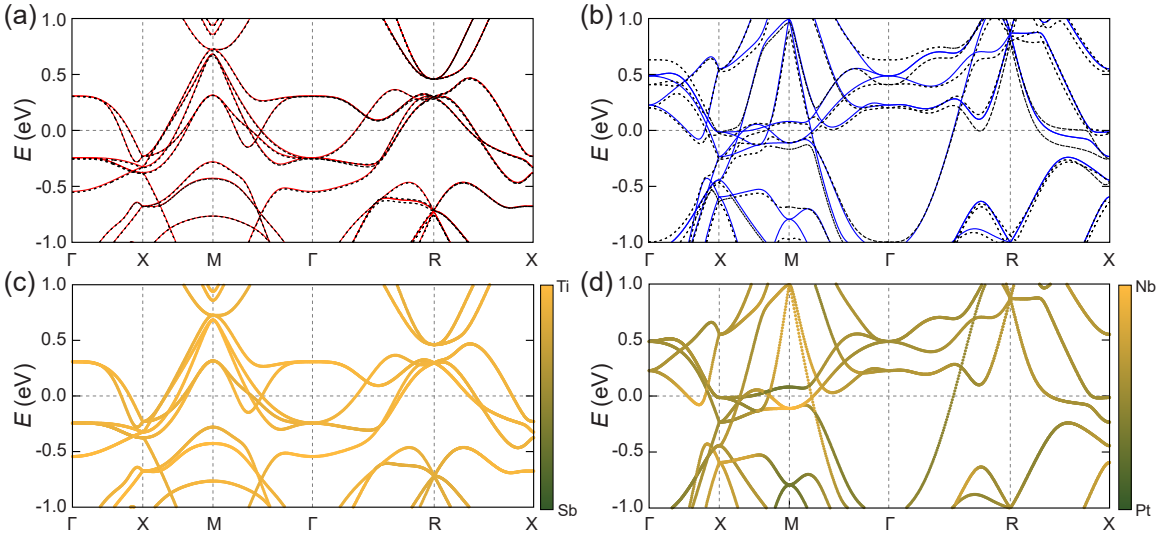

Fig. 2. The electronic band structures of (a) Ti_3Sb and (b) Nb_3Pt. The black dashed lines represent the calculations without SOC, while the red and blue solid lines represent the calculations with SOC. The orbital-resolved band structure of (c) Ti_3Sb and (d) Nb_3Pt. Ti and Nb atoms are weighted by 1/3 for comparison, reflecting their tippled quantity in each unit cell. The Fermi level set to zero.

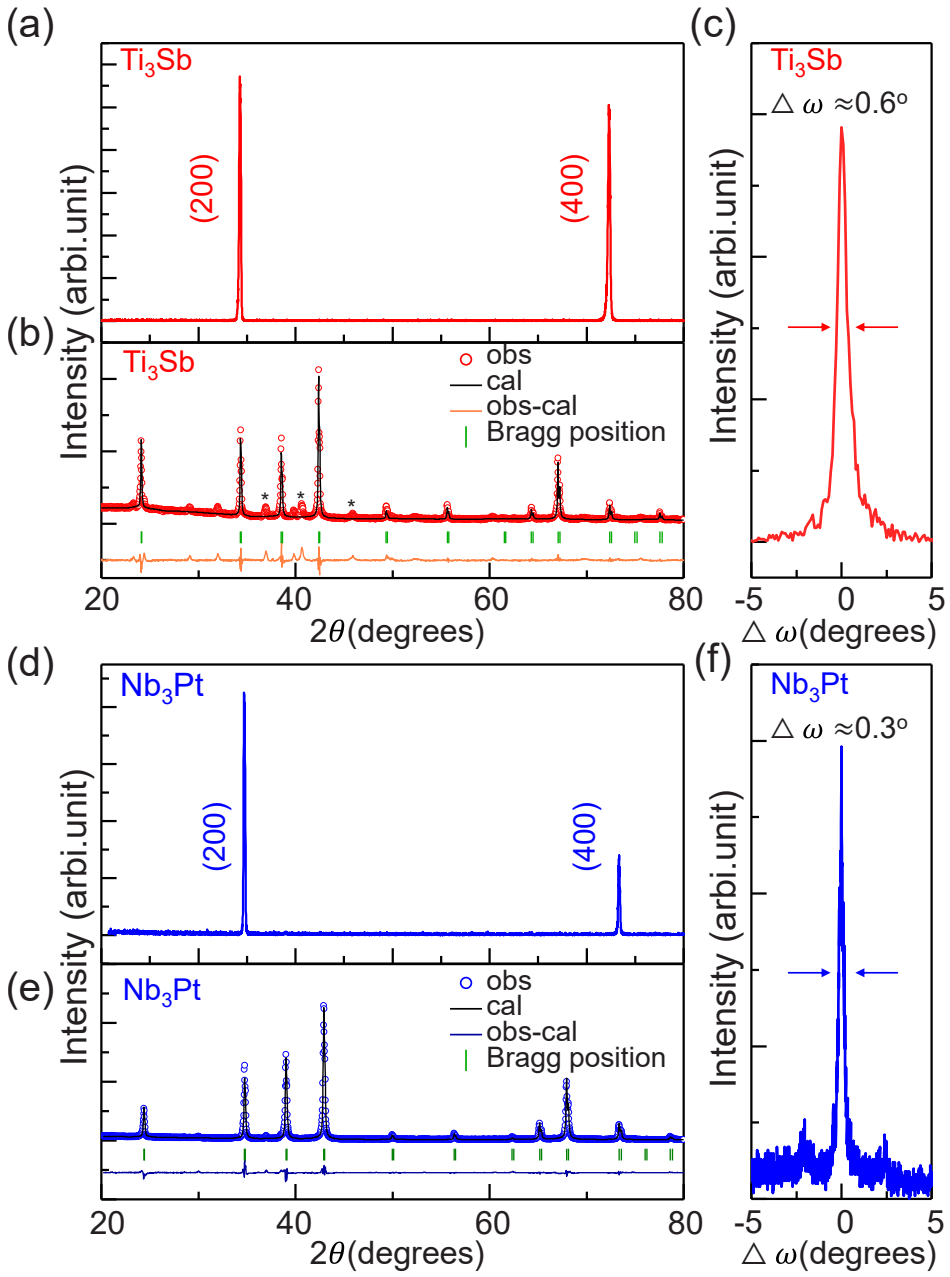

Fig. 3. (a, d) XRD patterns of Ti_3Sb and Nb_3Pt single crystals oriented along the [100] direction, showing distinct (200) and (400) Bragg reflections. (b, e) Rietveld refinement of the XRD patterns of the crushed single crystals of (b) Ti_3Sb and (e) Nb_3Pt. Red and blue circles represent the measured intensities, black lines denote the calculated patterns, and orange and blue lines indicate the differences between them. Vertical green bars mark the Bragg peak positions. The asterisks in Fig. 2(b) mark the peaks corresponding to traces of an impurity phase, Ti_2Sb. (c, f) Rocking curve measurements around the (200) reflection for Ti_3Sb and Nb_3Pt, respectively. The arrows in the figures indicate the positions corresponding to half of the maximum intensity, from which the FWHM values were determined.

Table 1
Refined lattice parameters of Ti_3Sb and Nb_3Pt.

	Ti_3Sb	Nb_3Pt
Data collection temperature (K)	300	
Space group	*Pm−3n*	
Lattice parameter (Å)	5.2127(1)	5.1652(1)
Unit cell volume (Å^3)	141.6407	137.8039
Radiation, wavelength (Å)	0.7093 (Mo K_α)	
Wyckoff position		
A(=Ti, Nb)	6c [(1/2, 1/4, 0)]	
B= (Sb, Pt)	2a [(1/2, 1/2, 1/2)]	

Fig. 4(a) and (b) show the temperature-dependent electrical resistivity of Ti_3Sb and Nb_3Pt single crystals, measured from 1.5 K to 300 K. A sharp drop in resistivity near $T_c \approx 6.5$ K for Ti_3Sb and $T_c \approx 8$ K for Nb_3Pt confirms the superconducting transition in both compounds, with transition temperatures consistent with previous studies [20,23]. Notably, the resistivity of the grown single crystals is higher than the values reported for annealed polycrystalline samples [21,23,24]. One possible explanation for this discrepancy is the presence of anti-site defects, where element B (e.g., Sb or Pt) occupies the A site (e.g., Ti or Nb). Previous studies have shown that stoichiometric samples tend to

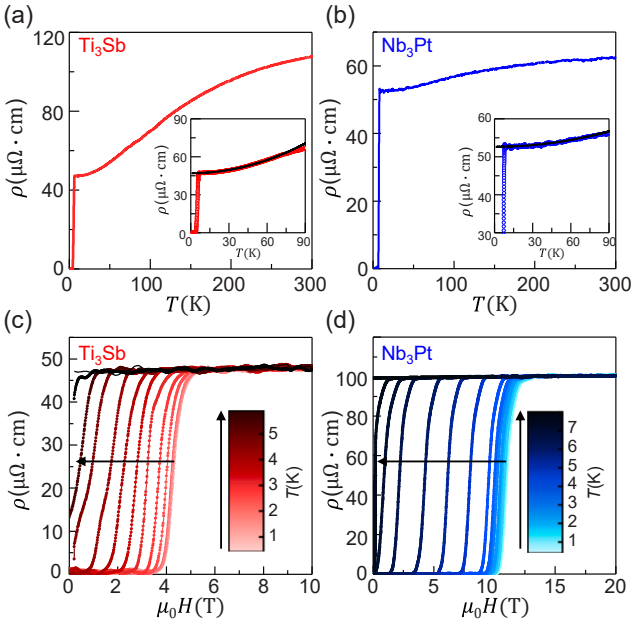

Fig. 4. (a, b) Temperature dependence of resistivity for (a) Ti_3Sb and (b) Nb_3Pt. Insets show the T^2 dependent resistivity fits below 90 K where the red and blue circles represent the experimental data and the black solid lines indicate the fitted curves. (c, d) Magnetic field dependent resistivity at various fixed temperatures from 0.4 K to T_c for (c) Ti_3Sb and (d) Nb_3Pt.

exhibit significantly lower resistivity than non-stoichiometric ones [25]. In particular, A-site-rich samples, which may have a high density of anti-site defects, exhibit a significant degradation in resistivity with an increasing A-site ratio [25]. Anti-site defects are known to form through quenching or neutron irradiation [26–28]. Given the rapid cooling inherent to the arc-melting process, the formation of anti-site defects may be promoted in the grown single crystal. An additional annealing process may help improve the conductivity of the sample by reducing anti-site defects, which will be explored in future work.

The single crystals exhibit residual resistivity ratio (RRR) values of $\rho(300K)/\rho(T_c) \approx$ 2.3 for Ti_3Sb and $\rho(300K)/\rho(T_c) \approx 1.2$ for Nb_3Pt. These values are comparable to previous reports [24,25]. At low temperature ($T < 90$ K), both single crystals show a T^2dependence of the resistivity as shown in the inset of Fig. 4(a) and (b). The black solid line represents the fitting with $\rho(T) = \rho_0 + AT^n$, where $n = 2$ [29,30]. The T^2dependence of resistivity at low temperatures suggests dominant electron-electron scattering [31], a characteristic commonly observed in high T_c superconductors [32] and A15-structured superconductors [30]. The coefficient A was found to be 0.0029 μΩ·cm/K^2 for Ti_3Sb and 0.0005 μΩ·cm/K^2 for Nb_3Pt, showing good agreement with previous reports obtained from polycrystalline samples [33].

Fig. 4(c) and (d) present the magnetic field-dependent resistivity of two different A15-structured superconducting compounds. Measurements were conducted at various temperatures, ranging from the base temperature of 0.4 K to just below T_c. Although only the upsweeps are plotted in Fig. 4(c) and (d), the field up- and down-sweeps produced almost identical curves. In the case of Ti_3Sb, a slight broadening of the superconducting transition was observed with increasing temperature, consistent with previously reported results [21]. Magnetic field-dependent resistivity measurements were performed on four different pieces of both Ti_3Sb(TS1–4) and Nb_3Pt(NP1–4), totaling eight samples, as shown in Fig. S7 in Supplementary material. Notably, the resistivity exhibited sample-to-sample variations, ranging from 45 to 100 μΩ·cm for Ti_3Sb and from 70 to 150 μΩ·cm for Nb_3Pt. These variations are likely attributable to differences in stoichiometry or defect distribution [23] and will be systematically investigated in future studies through additional annealing.

Using magnetic field-dependent resistivity data, $H_{c2}(T)$ was determined at different temperature (0.4 K $< T < T_c$). Here H_{c2} is defined as using the 50 % criterion of the normal-state resistivity, as shown in Fig. S8 in Supplementary material. The temperature dependence of $H_{c2}(T)$ obtained from a total of eight samples is shown in Fig. S9 in Supplementary material. The slope near T_c allows us to estimate the zero-temperature orbital upper critical field using the relation using $H_{c2}^{orb}(0) = -0.69|dH_{c2}/dT|_{T_c}T_c$ in the dirty limit [6]. This yields $H_{c2}^{orb}(0) \approx 5.1 \pm 0.2$ T for Ti_3Sb and $H_{c2}^{orb}(0) \approx 10.9 \pm 0.3$ T for Nb_3Pt as described in Table S1 in Supplementary material. The corresponding Ginzburg-Landau coherence lengths in the dirty limit are obtained as $\xi =$ 90.3 Å for Ti_3Sb and $\xi =$ 54.9 Å for Nb_3Pt. In addition to the orbital-limiting effect, the Pauli paramagnetic limit for a single gap in the weak coupling limit is given by $H_P(0) = 1.84T_c$, which results in $H_P(0) \approx 9.6 \pm 0.4$ T for Ti_3Sb and $H_P(0) \approx 12.6 \pm 0.3$ T for Nb_3Pt. Consequently, the Maki parameter for both compounds is estimated to be $\alpha \approx 0.7$ for Ti_3Sb and $\alpha \approx 1.2$ for Nb_3Pt.

By normalizing the obtained $H_{c2}(T)$ and T with respect to $H_{c2}^{orb}(0)$ and T_c, the normalized $H-T$ phase diagram is obtained, as shown in Fig. 5(a) and (b) for Ti_3Sb and Nb_3Pt, respectively. Here, $H_{c2}^{orb}(0)$ were estimated using representative slopes of 1.4 T/K for Ti_3Sb and 2.3 T/K for Nb_3Pt, which yield the best agreement with the WHH model, while T_c values were obtained by linear extrapolation of the resistive transition. To further investigate the contributions of orbital and Pauli paramagnetic effects to $H_{c2}(T)$, we first describe its temperature dependence using the WHH model [6], which is described by:

$$\ln\frac{1}{t} = \sum_{\nu=-\infty}^{\infty}\left\{\frac{1}{|2\nu+1|} - \left[|2\nu+1| + \frac{\hbar}{t} + \frac{\left(\frac{\alpha\hbar}{t}\right)^2}{|2\nu+1| + \frac{\hbar+\lambda_{SO}}{t}}\right]^{-1}\right\}$$

where $t = T/T_c$, $\hbar = (4/\pi^2)\left[H_{c2}(T)/|dH_{c2}/dT|_{T_c}\right]$, α is the Maki parameter, and λ_{SO} is the spin-orbit scattering parameter [6]. For Ti_3Sb single crystals as shown in Fig. 5(a), the experimental $H_{c2}(T)$ (closed symbols) at low temperature $T < 0.75T_c$ significantly deviates from the predictions of the WHH model considering orbital pair breaking only, i.e., $\alpha = 0$ (black solid line). This deviation is due to the Pauli-limiting effect, which flattens H_{c2} at low temperatures. The best fit of the WHH model, with a finite α, considering the Pauli-limiting effect, was obtained with $\alpha = 0.7$ (red solid line), which shows good agreement with the estimated value of with $\alpha \approx 0.7$ for Ti_3Sb using measured T_c and $|dH_{c2}/dT|_{T_c}$. It is noteworthy that spin-orbit scattering was not necessary for the best fit ($\lambda_{SO} = 0$), and this is consistent with DFT calculations, which showed that the SOC effect in Ti_3Sb is negligible.

A pronounced spin-orbit scattering effect was observed in Nb_3Pt. Compared to Ti_3Sb, Nb_3Pt exhibits a larger Maki parameter ($\alpha \approx 1.2$), suggesting that the Pauli limiting effect should suppress $H_{c2}(T)$, as shown by the blue dashed line in Fig. 5(b). However, experimental results reveal that, contrary to expectations, $H_{c2}(0)$ in Nb_3Pt approaches its orbital limiting field, $H_{c2}^{orb}(0)$ (black solid line). The discrepancy between the expected and experimental results is indicated by the gray arrow in Fig. 5(b). We attribute this discrepancy to the additional spin-orbit scattering effect. As predicted by the WHH model, spin-orbit scattering can restore the reduced $H_{c2}(T)$ due to the Pauli effect back toward its orbital limit. As shown in Fig. S10(a) in Supplementary material, when the Maki parameter is fixed at $\alpha = 1.2$ and the spin-orbit scattering effect (λ_{SO}) is increased, $H_{c2}(T)$ exhibits a recovery trend close to its orbital limit. This is consistent with the expectation that Nb_3Pt has strong spin-orbit scattering effects due to the influence of the 4*d* Nb and 5*d* Pt bands, as discussed in Fig. 1. The best fit to the experimental $H_{c2}(T)$ in Nb_3Pt was obtained $\alpha = 1.2$ with a sufficiently large $\lambda_{SO} > 10$ as shown by the violet solid line in Fig. 5(b). It is worth noting that while the exact value of λ_{SO} cannot be precisely determined,

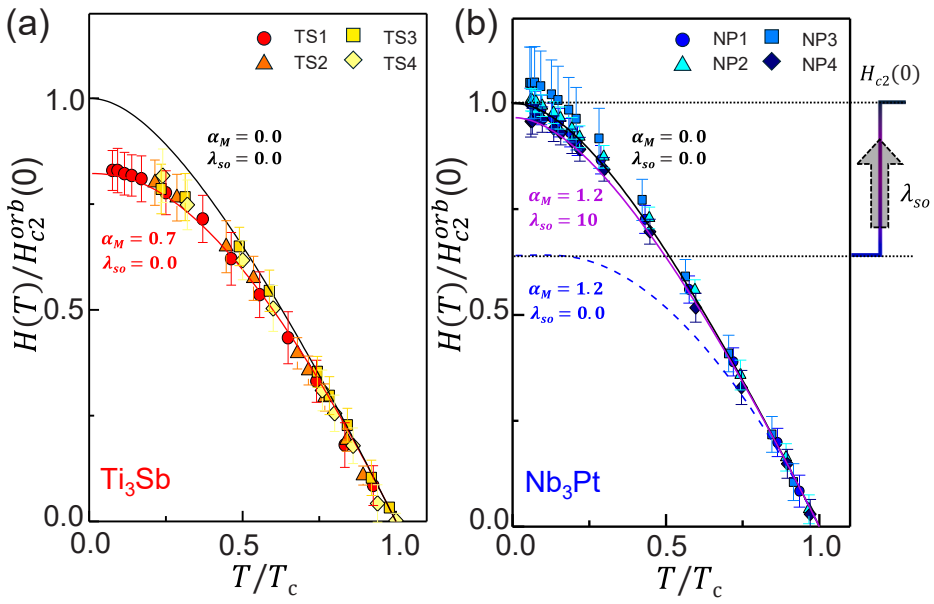

Fig. 5. Normalized Upper critical field $H_{c2}(T)/\ H_{c2}^{orb}(0)$, as a function of temperature for (a) Ti_3Sb and (b) Nb_3Pt. The scatter points represent the experimental data, while the black, red, and blue lines correspond to the WHH model fits with different α and λ_{SO} values. The black solid line represents the WHH model with only the orbital limiting effect, corresponding to $\alpha = 0$. The red solid line in (a) represents the fit with $\alpha = 0$ and without spin–orbit scattering ($\lambda_{SO} = 0$). The blue dashed line in (b) represents the WHH prediction with $\alpha = 1.2$, while the purple solid line is the fit with $\alpha = 1.2$ and $\lambda_{SO} = 10$, including λ_{SO} parameter.

we can establish the minimum value necessary to account for the experimental results. As λ_{SO} increases, $H_{c2}(T)$ exhibits a progressive recovery toward the orbital limit, ultimately reaching full restoration when λ_{SO} approaches infinity. Therefore, as discussed in Fig. S10(a) in the Supplementary material, considering the uncertainties associated with the experimental determination of $H_{c2}(T)$, the WHH model enables the identification of the minimum λ_{SO} value required to describe the observed $H_{c2}(T)$, within the experimental error range.

The estimated value of $\lambda_{SO} > 10$ is considered reasonable when compared to various superconducting materials. Table 2 presents a comparison of λ_{SO} values for different superconductors analyzed using the WHH model. In Fe-based superconductors, where 3*d* Fe electrons play a dominant role, spin-orbit scattering is negligible ($\lambda_{SO} \approx 0$), similar to what is observed in Ti_3Sb. In contrast, materials in which 4*d* or 5*d* electrons significantly contribute to superconductivity exhibit relatively large λ_{SO} value ($\lambda_{SO} > 1$). Another intriguing example is the Chevrel phase superconductors. As shown in Table 2, superconductors composed of elements with increasing SOC strength—Cu (3*d*), Sn (5*p*), and Pb (6*p*)—exhibit a corresponding increase in the effect of λ_{SO} on $H_{c2}(T)$. This trend aligns well with our observations in A15-structured superconductors, reinforcing the understanding that SOC serves as a crucial tuning parameter in optimizing $H_{c2}(T)$ in superconductors.

4. Conclusion

In this study, we systematically investigated the role of SOC in superconductivity by synthesizing A15-structured single crystals of Ti_3Sb and Nb_3Pt using the tetra-arc Czochralski method. Despite their identical crystal structure, these compounds exhibit distinct SOC strengths, providing an ideal platform for studying its effects on superconductivy. The $T_c$of Ti_3Sb and Nb_3Pt were measured to be 6.5 K and 8 K, respectively, in agreement gf with previous reports. The $H_{c2}(T)$ curves at low

Table 2
Comparison of superconducting and spin-orbit coupling parameters in various superconductors. The table also provides the sample type, orbital contribution of the constituent elements, critical temperature T_c and maki parameter α. The valence orbitals of constituent elements are color-coded by their principal quantum number (n), with black ($n = 2$), red ($n = 3$), green ($n = 4$), blue ($n = 5$), and violet ($n = 6$). Superconductors containing elements with larger atomic numbers (Z), corresseponding to higher pricipal quantum number (n), tend to exhibit larger λ_{SO}.

Compound		Sample Type	Orbital Contribution	T_c (K)	α	λ_{so}	ref
Fe-based SC	FeSe	Single crystal	Fe(3*d*), Se(4*p*)	9	1.5	0	[34]
	LiFeAs	Single crystal	Fe(3*d*), As(4*p*)	18	0.9	0	[35]
	$Ba(Fe_{0.92}Co_{0.08})_2As_2$	Thin film	Fe(3*d*), As(4*p*)	25.8	1.25	0.5	[36]
	Sr_2VO_3FeAs	Single crystal	Fe(3*d*), As(4*p*)	30	4	0	[37]
	$Ti_{0.88}Mn_{0.12}$	Polycrystalline	Ti(3*d*), Mn(3*d*)	24	2.06	0	[38]
	$Cs_2Cr_3As_3$	Single crystal	Cr(3*d*), As(4*p*), Cs(6 *s*)	2.2	1.8	0.25	[39]
	$RbOs_2O_6$	Single crystals	Os(5*d*), O(2*p*), Rb(5 *s*)	5.50	0.75	1.3	[40]
	NbS_2	Single crystals	Nb(4*d*), S(3*p*)	6	6	1	[41]
	$Sr_3Ir_4Sn_{13}$	Single crystal	Ir(5*d*), Sn(5*p*), Sr(5 *s*)	5	0.528	1.4	[42]
	$Ta_2V_{3.1}Si_{0.9}$	Polycrystalline	V(3*d*), Ta(4*d*), Si(3*p*)	7.5	1.62	2.2	[43]
	$ThPt_3B$	Single crystal	Pt(5*d*), Th(6*d*), B(2*p*)	0.75	0.57	15	[44]
	Re_6Zr	Polycrystalline	Re(5*d*), Zr(4*d*)	6.75	1.31	18	[45]
Chevrel Phase SC	$Cu_2Mo_6S_8$	Polycrystalline	Cu(3*d*), Mo(4*d*), S(3*p*)	4.3	2.25	0	[46]
	$Sn_{1.2}Mo_{6.35}S_8$	Single crystal	Mo(4*d*), Sn(5*p*), S(3*p*)	12.3	2.4	13	[46]
	$PbMo_{6.35}S_8$	Single crystal	Mo(4*d*), Pb(6*p*), S(3*p*)	13.3	3.25	∞	[46]

temperature were fitted using WHH model, enabling an analysis of the influence of paramagnetic limiting and SOC strength on superconducting properties. Notably, a strong spin-orbit scattering effect was found to impact superconducting pair breaking mechanisms, effectively enhancing $H_{c2}(T)$ close to the orbital limit. These results highlight SOC as a key factor in optimizing superconducting properties, offering valuable insights for designing next-generation superconductors, including high-performance superconducting wires and topological superconductors.

CRediT authorship contribution statement

Eun Sang Choi: Writing – review & editing, Investigation. **Huiwon Kim:** Writing – review & editing, Investigation. **Min Jae Kim:** Writing – review & editing, Investigation. **Jong Mok Ok:** Writing – review & editing, Writing – original draft, Project administration, Investigation, Funding acquisition, Conceptualization. **Jeongwoo Kim:** Writing – review & editing, Visualization, Software, Investigation. **Sangmoon Yoon:** Writing – review & editing, Investigation. **Youngji Cho:** Writing – review & editing, Investigation. **Minsik Kong:** Writing – review & editing, Investigation. **Gichan Son:** Writing – review & editing, Software, Investigation. **Seohee Kim:** Writing – original draft, Visualization, Software, Resources, Investigation, Formal analysis, Data curation.

Declaration of Competing Interest

The authors declare that they have no known competing financial interests or personal relationships that could have appeared to influence the work reported in this paper

Acknowledgements

This work was supported by the Nano & Material Technology Development Program through the National Research Foundation of Korea(NRF) funded by Ministry of Science and ICT (RS-2023-00281839), the National Research Foundation of Korea(NRF) grant funded by the Korea government (MSTI) (No. RS-2023-00210295, No. RS-2023-00221154, RS-2022-NR068578, No. RS-2024-00410027), and the IITP (Institute of Information & Communications Technology Planning & Evaluation)-ITRC(Information Technology Research Center) grant funded by the Korea government (Ministry of Science and ICT) (IITP-2025-RS-2020-II201606)

Appendix A. Supporting information

Supplementary data associated with this article can be found in the online version at doi:10.1016/j.jallcom.2025.182350.

References

[1] J.E. Moore, The birth of topological insulators, Nature 464 (2010) 194–198, https://doi.org/10.1038/nature08916.
[2] J. Sinova, S.O. Valenzuela, J. Wunderlich, C. Back, T. Jungwirth, Spin hall effects, Rev. Mod. Phys. 87 (2015) 1213–1260, https://doi.org/10.1103/RevModPhys.87.1213.
[3] E. Rashba, V. Sheka, Symmetry of energy bands in crystals of wurtzite type, Sov. Phys. Solid State 1 (1959) 368–380, https://doi.org/10.1103/PhysRevB.106.230001.
[4] X.-L. Qi, S.-C. Zhang, Topological insulators and superconductors, Rev. Mod. Phys. 83 (2011) 1057–1110, https://doi.org/10.1103/RevModPhys.83.1057.
[5] M. Zeng, D.-H. Xu, Z.-M. Wang, L.-H. Hu, Spin-orbit coupled superconductivity with spin-singlet nonunitary pairing, Phys. Rev. B 107 (2023) 094507, https://doi.org/10.1103/PhysRevB.107.094507.
[6] N. Werthamer, E. Helfand, P. Hohenberg, Temperature and purity dependence of the superconducting critical field, H_{c2}. III. Electron spin and spin-orbit effects, Phys. Rev. 147 (1966) 295, https://doi.org/10.1103/PhysRev.147.295.
[7] G.R. Stewart, Superconductivity in the A15 structure, Physica C Superconductivity Applications 514 (2015) 28–35, https://doi.org/10.1016/j.physc.2015.02.013.
[8] B. Matthias, T. Geballe, S. Geller, E. Corenzwit, Superconductivity of Nb_3Sn, Phys. Rev. 95 (1954) 1435, https://doi.org/10.1103/PhysRev.95.1435.
[9] L. Newkirk, F. Valencia, A. Giorgi, E. Szklarz, T. Wallace, Bulk superconductivity above 20 K in Nb_3Ge, IEEE Trans. Magn. 11 (1975) 221–224, https://doi.org/10.1109/TMAG.1975.1058637s.
[10] X. Xu, A review and prospects for Nb_3Sn superconductor development, Supercond. Sci. Technol. 30 (2017) 093001, https://doi.org/10.1088/1361-6668/aa7976.
[11] M. Kim, C.-Z. Wang, K.-M. Ho, Topological states in A15 superconductors, Phys. Rev. B 99 (2019) 224506, https://doi.org/10.1103/PhysRevB.99.224506.
[12] R.M. Sattigeri, G. Cuono, G. Hussain, X. Ming, A. Di Bernardo, C. Attanasio, M. Cuoco, C. Autieri, Dirac surface states, multiorbital dimerization, and superconductivity in Nb-and Ta-based A15 compounds, Phys. Rev. B 109 (2024) 075119, https://doi.org/10.1103/PhysRevB.109.075119.
[13] M. Kong, M. Kang, G. Ji, S. Park, B. Choe, J.M. Ok, Large-size single crystal growth for quantum materials by Czochraski method, Curr. Appl. Phys. (2024), https://doi.org/10.1016/j.cap.2024.02.007.
[14] P.E. Blöchl, Projector augmented-wave method, Phys. Rev. B 50 (1994) 17953, https://doi.org/10.1103/PhysRevB.50.17953.
[15] G. Kresse, D. Joubert, From ultrasoft pseudopotentials to the projector augmented-wave method, Phys. Rev. b 59 (1999) 1758, https://doi.org/10.1103/PhysRevB.59.1758.
[16] G. Kresse, Furthmüller, Phys. Rev. B 54 (1996) (1996) 1169, https://doi.org/10.1103/PhysRevB.54.11169.
[17] J.P. Perdew, K. Burke, M. Ernzerhof, Generalized gradient approximation made simple, Phys. Rev. Lett. 77 (1996) 3865, https://doi.org/10.1103/PhysRevLett.77.3865.
[18] M. Tinkham, Introduction to Superconductivity, Courier Corporation, 2004.
[19] A.M. Clogston, Upper limit for the critical field in hard superconductors, Phys. Rev. Lett. 9 (1962) 266, https://doi.org/10.1103/PhysRevLett.9.266.
[20] K. Maki, Effect of Pauli paramagnetism on magnetic properties of high-field superconductors, Phys. Rev. 148 (1966) 362, https://doi.org/10.1103/PhysRev.148.362.
[21] R. Chapai, M. Smylie, H. Hebbeker, D. Chung, W.-K. Kwok, J. Mitchell, U. Welp, Superconducting properties and gap structure of the topological superconductor candidate Ti_3Sb, Phys. Rev. B 107 (2023) 104504, https://doi.org/10.1103/PhysRevB.107.104504.
[22] R. Flükiger, S. Foner, E. McNiff, Jr, Ø. Fischer, Upper critical fields of $Nb_{-3}Au$, $Nb_3Au_{0.7}Pt_{0.3}$ and Nb_3Pt, Solid State Commun. 30 (1979) 723–726, https://doi.org/10.1016/0038-1098(79)91169-4.
[23] D. Dew-Hughes, R. Caton, R. Jones, D.O. Welch, Recovery of Tc by annealing in disordered Nb3Pt. Superconductivity in D-and F-Band Metals, Elsevier, 1980, pp. 355–361, https://doi.org/10.1016/B978-0-12-676150-4.50043-3.
[24] M. Mandal, S. KP, R.R. Chowdhury, D. Singh, P. Biswas, A. Hillier, R. Singh, Superconducting ground state of the topological superconducting candidates Ti_3X (X= Ir, Sb), Phys. Rev. B 103 (2021) 054501, https://doi.org/10.1103/PhysRevB.103.054501.
[25] S. Moehlecke, H. Borges, C. Santos, A. Sweedler, Resistivity as a function of composition in the superconducting Nb-Pt A15 phase, J. Low. Temp. Phys. 70 (1988) 449–457, https://doi.org/10.1007/BF00682158.
[26] R. Blaugher, R. Hein, J. Cox, R. Waterstrat, Atomic ordering and superconductivity in A-15 compounds, J. Low. Temp. Phys. 1 (1969) 539–561, https://doi.org/10.1007/BF00627932.
[27] H. Kodaka, K. Miyata, H. Yoshida, H. Yamaoka, M. Fukumoto, T. Okada, Neutron irradiation effects on critical temperatures of A15-type superconducting composites, J. Nucl. Mater. 133 (1985) 819–822, https://doi.org/10.1016/0022-3115(85)90265-X.
[28] S. Moehlecke, D. Cox, A. Sweedler, The effects of neutron irradiation on the superconducting properties of Nb_3Pt, J. Less Common Met. 62 (1978) 111–118, https://doi.org/10.1016/0022-5088(78)90020-6.
[29] R. Caton, R. Viswanathan, Analysis of the normal-state resistivity for the neutron-irradiated A15 superconductors V_3Si, Nb_3Pt, and Nb_3Al, Phys. Rev. B 25 (1982) 179.
[30] M. Gurvitch, A. Ghosh, H. Lutz, M. Strongin, Low-temperature resistivity of ordered and disordered A 5 compounds, Phys. Rev. B 22 (1980) 128, https://doi.org/10.1103/PhysRevB.25.179.
[31] M. Kaveh, N. Wiser, Electron-electron scattering in conducting materials, Adv. Phys. 33 (1984) 257–372, https://doi.org/10.1080/00018738400101671.
[32] G. Webb, Z. Fisk, J. Engelhardt, S. Bader, Apparent T^2 dependence of the normal-state resistivities and lattice heat capacities of high-T_c superconductors, Phys. Rev. B 15 (1977) 2624, https://doi.org/10.1103/PhysRevB.15.2624.
[33] S. Ramakrishnan, G. Chandra, Normal state resistivity and Tç studies of superconducting $Ti_{1-x}Sb_x$ system, Phys. Lett. A 100 (1984) 441–444, https://doi.org/10.1016/0375-9601(84)90640-6.
[34] J.M. Ok, C.I. Kwon, Y. Kohama, J.S. You, S.K. Park, J.-h Kim, Y. Jo, E. Choi, K. Kindo, W. Kang, Observation of in-plane magnetic field induced phase transitions in FeSe, Phys. Rev. B 101 (2020) 224509, https://doi.org/10.1103/PhysRevB.101.224509.
[35] S. Khim, B. Lee, J.W. Kim, E.S. Choi, G. Stewart, K.H. Kim, Pauli-limiting effects in the upper critical fields of a clean LiFeAs single crystal, Phys. Rev. BCondens. Matter Mater. Phys. 84 (2011) 104502, https://doi.org/10.1103/PhysRevB.84.104502.
[36] J. Hänisch, K. Iida, F. Kurth, E. Reich, C. Tarantini, J. Jaroszynski, T. Förster, G. Fuchs, R. Hühne, V. Grinenko, High field superconducting properties of Ba $(Fe_{1-x}Co_x)_2As_2$ thin films, Sci. Rep. 5 (2015) 17363, https://doi.org/10.1038/srep17363.
[37] J.M. Ok, C.I. Kwon, O.A. Valenzuela, S. Kim, R.D. McDonald, J. Kim, E. Choi, W. Kang, Y. Jo, C. Kim, Strong antiferromagnetic proximity coupling in the

heterostructure superconductor $Sr_2VO_{3-\delta}FeAs$, Phys. Rev. B 105 (2022) 214505, https://doi.org/10.1103/PhysRevB.105.214505.
[38] Y.-J. Zhang, Q. Li, Z. Zhu, Y. Li, W. Xie, H.-H. Wen, Enhanced superconductivity in $Ti_{1-x}Mn_x$ alloys through Mn doping, Phys. Rev. B 108 (2023) 054516, https://doi.org/10.1103/PhysRevB.108.054516.
[39] G.-H. Cao, Z.-W. Zhu, Superconductivity with peculiar upper critical fields in quasi-one-dimensional Cr-based pnictides, Chin. Phys. B 27 (2018) 107401, https://doi.org/10.1088/1674-1056/27/10/107401.
[40] P. Legendre, Y. Fasano, I. Maggio-Aprile, Ø. Fischer, Z. Bukowski, S. Katrych, J. Karpinski, Unexpectedly wide reversible vortex region in β-pyrochlore $RbOs_2O_6$: bulk magnetization measurements, Phys. Rev. BCondens. Matter Mater. Phys. 78 (2008) 144513, https://doi.org/10.1103/PhysRevB.78.144513.
[41] D. Pizzirani, T. Ottenbros, M. van Rijssel, O. Zheliuk, Y. Kreminska, M. Rösner, J. Linnartz, A. de Visser, N. Hussey, J. Ye, From orbital to paramagnetic pair breaking in layered superconductor 2H-NbS_2, Phys. Rev. Res. 6 (2024) L042006, https://doi.org/10.1103/PhysRevResearch.6.L042006.
[42] P. Biswas, A. Amato, R. Khasanov, H. Luetkens, K. Wang, C. Petrovic, R.M. Cook, M.R. Lees, E. Morenzoni, Superconducting and magnetic properties of $Sr_3Ir_4Sn_{13}$, Phys. Rev. B 90 (2014) 144505, https://doi.org/10.1103/PhysRevB.90.144505.
[43] H. Liu, J. Yao, J. Shi, Z. Yang, D. Yan, Y. Li, D. Chen, H.L. Feng, S. Li, Z. Wang, Vanadium-based superconductivity in the breathing kagome compound $Ta_2V_{3.1}Si_{0.9}$, Phys. Rev. B 108 (2023) 104504, https://doi.org/10.1103/PhysRevB.108.104504.
[44] E. Bauer, E. Royanian, H. Michor, O. Sologub, E.-W. Scheidt, A. Gonçalves, J. Bursik, W. Wolf, D. Reith, C. Blaas-Schenner, Superconductivity and spin fluctuations in the actinoid–platinum metal borides {Th, U}Pt_3B, Phys. Rev. B 92 (2015) 024511, https://doi.org/10.1103/PhysRevB.92.024511.
[45] D. Mayoh, J. Barker, R. Singh, G. Balakrishnan, D.M. Paul, M.R. Lees, Superconducting and normal-state properties of the noncentrosymmetric superconductor Re_6Zr, Phys. Rev. B 96 (2017) 064521, https://doi.org/10.1103/PhysRevB.96.064521.
[46] Y. KIMURA, J. Cryog. Soc. Jpn. 14 (1979) 51–63, https://doi.org/10.2221/jcsj.14.51.